Atomistic mechanisms of amorphization during nanoindentation of SiC: A molecular dynamics study

Izabela Szlufarska,[1] Rajiv K. Kalia,[2] Aiichiro Nakano,[2] and Priya Vashishta[2]
[1]*Department of Materials Science and Engineering, University of Wisconsin-Madison, Madison, Wisconsin 53706-1595, USA*
[2]*Collaboratory for Advanced Computing and Simulations, Department of Materials Science & Engineering, Department of Computer Science, Department of Physics & Astronomy, and Department of Biomedical Engineering, University of Southern California, Los Angeles, California 90089-0242, USA*
(Received 27 May 2004; published 26 May 2005)

Atomistic mechanisms underlying the nanoindentation-induced amorphization in SiC crystal has been studied by molecular dynamics simulations on parallel computers. The calculated load-displacement curve consists of a series of load drops, corresponding to plastic deformation, in addition to a shoulder at a smaller displacement, which is fully reversible upon unloading. The peaks in the load-displacement curve are shown to reflect the crystalline structure and dislocation activities under the surface. The evolution of indentation damage and defect accumulation are also discussed in terms of bond angles, local pressure, local shear stress, and spatial rearrangements of atoms. These structural analyses reveal that the defect-stimulated growth and coalescence of dislocation loops are responsible for the crystalline-to-amorphous transition. The shortest-path-ring analysis is effectively employed to characterize nanoindentation-induced structural transformations and dislocation activities.

DOI: 10.1103/PhysRevB.71.174113 PACS number(s): 81.70.Bt, 62.20.Fe, 64.70.Kb, 02.70.Ns

I. INTRODUCTION

Silicon carbide (SiC) is a promising candidate for a variety of technological applications, e.g., in optoelectronic devices and engineering materials. Its application is driven by such outstanding physical and chemical properties as light weight, high stiffness, and high hardness at high temperatures; excellent high-temperature resistance to fracture, creep and corrosion; chemical stability; and low thermal expansion. The high barrier for electric breakdown, high electron mobility, wide band gap, and high thermal conductivity make SiC suitable for radar and microwave application under extreme conditions.[1] SiC is already used in gas turbines, heat exchangers, and ceramic fans;[2] it is also expected to improve the design of high-voltage switching[3–5] as well as sensors and controls for cleaner-burning, more fuel-efficient jet aircraft and automobile engines.[6,7] SiC occurs in many different crystal structures originating from differences in the stacking sequence of the silicon-carbon bilayers.[8,9] The most common is the cubic polytype (zinc-blende structure) denoted as 3C—SiC.

For reliability and durability of SiC in structural and device applications, testing of mechanical stability is essential. Indentation is a unique local probe of mechanical properties of materials,[10–16] especially at surfaces and thin films, and it is widely used to assess the mechanical stability of structural components. When a sharp indenter is loaded into a solid, it generates an extremely high stress, which often gives rise to a solid-state amorphization. Since the first experimental report by Clarke *et al.*[13] of indentation-induced crystalline to amorphous ($c \rightarrow a$) transition in silicon and germanium, similar phenomena have been observed in other experiments[12,17–19] as well as in computer simulations.[20,21] Despite these efforts, atomistic mechanisms of the indentation-induced $c \rightarrow a$ transformation are still not fully understood.

Several experimental[18,22–26] and theoretical[27–31] results suggest correlations between the nanoindentation load-displacement (P-h) response and the deformation structures in materials. Page *et al.*[22] noted a pop-in behavior in the P-h curves of Al_2O_3 and 6H—SiC, which was related to the nucleation of subsurface defects, i.e., dislocations and dislocation loops. Recent transmission electron microscopy (TEM) measurement by Tachi *et al.*[18] provided evidence that dislocation activity leads to amorphization during indentation of silicon. However, the atomistic mechanism of amorphization was not proposed.

The $c \rightarrow a$ transformation is initiated on the atomic scale and hence, to fully characterize the onset of plasticity, one cannot rely solely on continuum concepts, such as critical shear stress, yield strength, or hardness. Though scanning electron microscopy (SEM), scanning tunneling microscopy (STM), atomic force microscopy (AFM), and TEM techniques, used in nanoindentation experiments, are able to detect dislocations, it is difficult to resolve detailed atomistic structures and dynamics of defects.[22] Atomistic simulations based on the molecular dynamics[32] (MD) method provide trajectories of all the atoms and have been previously employed to study the subsurface structure deformations at the onset of plasticity in indented metals[27,31,33–37] and ceramics.[38] The MD method has also been combined with continuum schemes, which allowed for the modeling of systems with dimensions of the order of microns. For example, a hybrid MD–finite-element simulation approach to nanoindentation by Shenoy *et al.*[39] and Tadmor *et al.*[40] brought a great insight into the mechanisms of dislocation nucleation at the initial stages of plastic activity. MD simulations are thus expected to shed some light on the atomistic pathway to indentation-induced amorphization.

In this paper we present MD study of the atomistic mechanisms leading to amorphization of 3C—SiC via

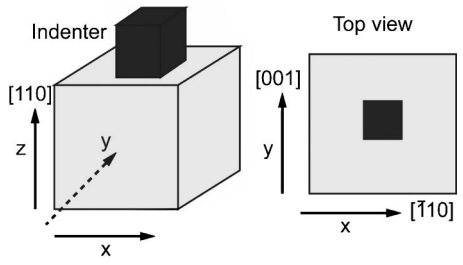

FIG. 1. A schematic view of the indenter-substrate system. The substrate has dimensions 308.3 Å × 309.5 Å × 107.9 Å in the *x*, *y*, and *z* directions, and has 994 000 atoms. The *x* and *y* axes correspond to the [$\bar{1}$10] and [001] crystallographic directions, respectively. The indent was done on the (110) surface.

nanoindentation. We observe a reversible pop-in behavior in the *P*-*h* response, which suggests an elastic recovery of 3C—SiC. In the plastic range of the *P*-*h* curve, we observe a series of load drops and show their relation to subsurface dislocation activities. The occurrence of the discontinuities at particular indentation depths is explained in terms of atomic spacing and strength of the crystal. We show that the defect-stimulated growth and merging of low-mobility dislocation loops play an important role in indentation-induced amorphization.

In our study the evolution of dislocations is characterized by means of atomic positions, shear stress, local pressure, bond angle, and shortest-path ring distributions. We show how the bond angle distribution evolves with the increasing indentation depth until it resembles that of a melt-quenched amorphous state. Following an early experimental observation[22] of dislocation loops creating an indentation at near to the theoretical strength, there was a number of theoretical studies in which the dislocations were visualized by means of the centrosymmetry parameter[27] and coordination number.[28] It has been long known that crystalline and disordered structures may also be characterized by distribution of rings defined by shortest-path analysis.[41–43]

II. METHODOLOGY

A. Molecular dynamics

In MD simulations the physical system is described by sets of N atomic positions $\{\vec{r}_i | i=1,\ldots,N\}$ and velocities $\{\vec{v}_i | i=1,\ldots,N\}$. We discretize time into discrete intervals Δt and numerically solve Newton's equations of motion with a potential $V(\{\vec{r}_i\})$,

$$m_i \frac{\mathrm{d}^2 \vec{r}_i(t)}{\mathrm{d}t^2} = -\frac{\partial V}{\partial \vec{r}_i}. \tag{1}$$

The nanoindentation simulation of 3C—SiC is performed by means of isothermal MD method.[44–46] The equations of motion are integrated by a reversible symplectic algorithm[44,47] with a time step of $\Delta t = 2.2$ fs.

The essential ingredient of MD is a reliable interaction potential. Our interatomic potential consists of two- and three-body terms,[48,49]

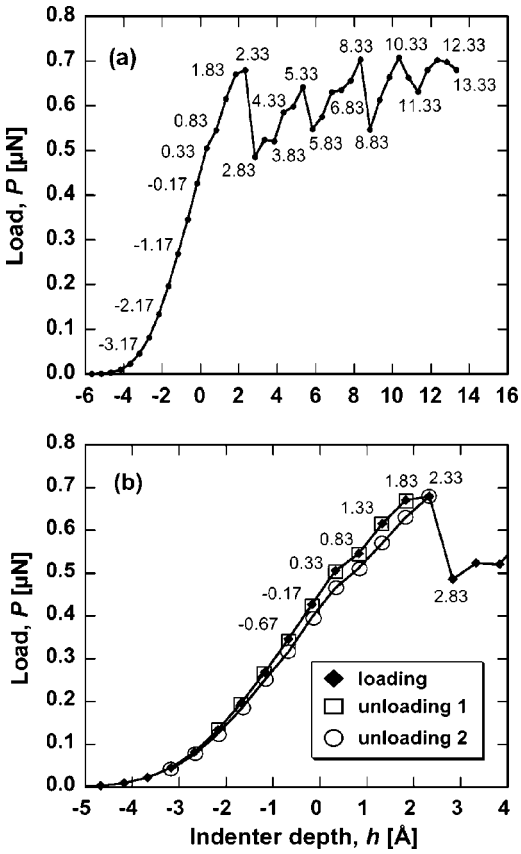

FIG. 2. Load-displacement (*P*-*h*) response: (a) Loading curve. (b) Unloading curves from $h=1.83$ Å (squares) and $h=2.33$ Å (circles) superimposed on the loading curve. Note different scales on the horizontal axes in (a) and (b).

$$V = \sum_{i<j} V_{ij}^{(2)}(r_{ij}) + \sum_{i,j<k} V_{jik}^{(3)}(\vec{r}_{ij}, \vec{r}_{ik}), \tag{2}$$

where $r_{ij} = |\vec{r}_{ij}|$ and $\vec{r}_{ij} = \vec{r}_i - \vec{r}_j$. The two-body potential is given by

$$V_{ij}^{(2)}(r_{ij}) = \frac{H_{ij}}{r_{ij}^{n_{ij}}} + \frac{Z_i Z_j}{r_{ij}} e^{-r_{ij}/a} - \frac{1}{2}\frac{(\alpha_i Z_j^2 + \alpha_j Z_i^2)}{r_{ij}^4} e^{-r_{ij}/b} - \frac{W_{ij}}{r_{ij}^6}, \tag{3}$$

in which the four terms describe steric repulsion, charge transfer between atoms, charge-dipole interactions, and van der Waals interactions, respectively. In Eq. (3), H_{ij}, n_{ij}, and W_{ij} are parameters, Z_i is the effective atomic charge, a and b are screening parameters, and α_i is the polarizability. Covalent effects are taken into account through three-body bond-bending and bond-stretching terms

$$V_{jik}^{(3)}(\vec{r}_{ij}, \vec{r}_{ik}) = B_{jik} \exp\left(\frac{\gamma}{r_{ij} - r_0} + \frac{\gamma}{r_{ik} - r_0}\right) \times \frac{(\cos\theta_{jik} - \cos\overline{\theta}_{jik})^2}{1 + C(\cos\theta_{jik} - \cos\overline{\theta}_{jik})^2} \times \Theta(r_0 - r_{ij})\Theta(r_0 - r_{ik}), \tag{4}$$

where B_{jik} is the strength of the interaction, $\Theta(t) = 1$ $(t \geq 0)$

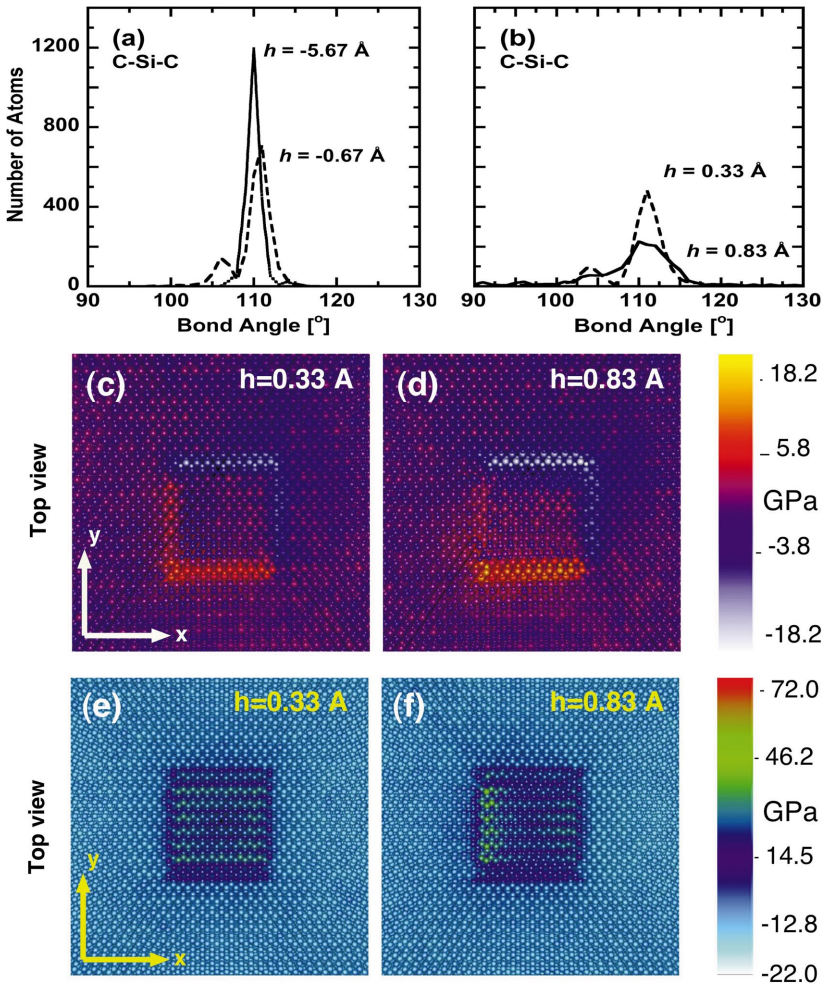

FIG. 3. (Color) Structural changes at the elastic shoulder: (a,b) Bond angle distribution of substrate atoms down to 12 Å below the initial surface at indenter depths $h=-5.67$ Å, $h=-0.67$ Å, $h=0.33$ Å, and $h=0.83$ Å. (c,d) Surface view of shear stress at $h=0.33$ Å and $h=0.83$ Å. (e,f) Surface view of pressure (as defined in Sec. III B) at $h=0.33$ Å and $h=0.83$ Å.

and 0 ($t<0$), $\theta_{jik}=\vec{r}_{ij}\cdot\vec{r}_{ik}/r_{ij}r_{ik}$ is the bond angle, and $\overline{\theta}_{jik}$, C, r_0, and γ are parameters. Calculated lattice constant, melting temperature, and elastic constants[43,50,51] are in excellent agreement with experiments.[52,53] The same potential parameters were used earlier to correctly describe reversible structural transformation of SiC under pressure.[50] In fact, our MD study predicted a zinc-blende–to–rocksalt transition mechanism, which was later confirmed by first-principles calculations.[54]

B. Simulation setup and schedule

The simulated 3C—SiC crystal has lateral dimensions of 308.3 Å$\times$309.5 Å in the x and y directions, corresponding to the $[\bar{1}10]$ and [001] crystallographic directions, respectively. The crystal has a thickness of 107.9 Å in the [110] direction (the z axis) and consists of 994 000 atoms. Periodic boundary conditions (PBC) are applied in the x and y directions. A schematic of the MD simulation is shown in Fig. 1. Starting with an ideal zinc-blende structure at $T=300$ K, a bulk of SiC is cooled down over $7200\Delta t$ to $T=0$ K, where potential energy is minimized by means of the conjugate gradient method. After removing PBC in the z direction (the indent direction) and freezing the bottom 12 Å of the crystal, the conjugate gradient method is applied again, and then the temperature is slowly raised to 300 K over $43\,000\Delta t$. The SiC indenter has a cuboidal shape, i.e., it has a flat base with a rectangular cross section of dimensions 30.8 Å$\times$30.5 Å and a height of $\sim$60 Å. For simplicity, the indenter is held rigid and only the steric repulsion is considered between indenter atoms and the substrate.

The indenter is inserted up to a maximum depth, which is $\sim$10% of the substrate thickness, at a rate of 1 Å per $500\Delta t$. Each 0.5 Å increment of the indenter depth is followed by a holding phase (on the average $6000\Delta t$). During this phase the transient forces are monitored and allowed to decay. The load P is calculated as the z component of the force exerted on the indenter by the substrate averaged over one to two periods of the force oscillations. The indentation depth h is calculated as the difference between the lowest point of the rigid indenter and the initial position of the substrate-free surface. A total of 375 000 MD steps is performed during the loading and unloading phases.

The simulation has been carried out on the 422-processor Linux cluster connected via Myrinet and gigabit/fast Ethernet switches at the Collaboratory for Advanced Computing and Simulations at the University of Southern California. A typical run uses 32 processors of the Linux cluster. The communication is handled with the Argonne implementation of the Message-Passing Interface, MPICH.

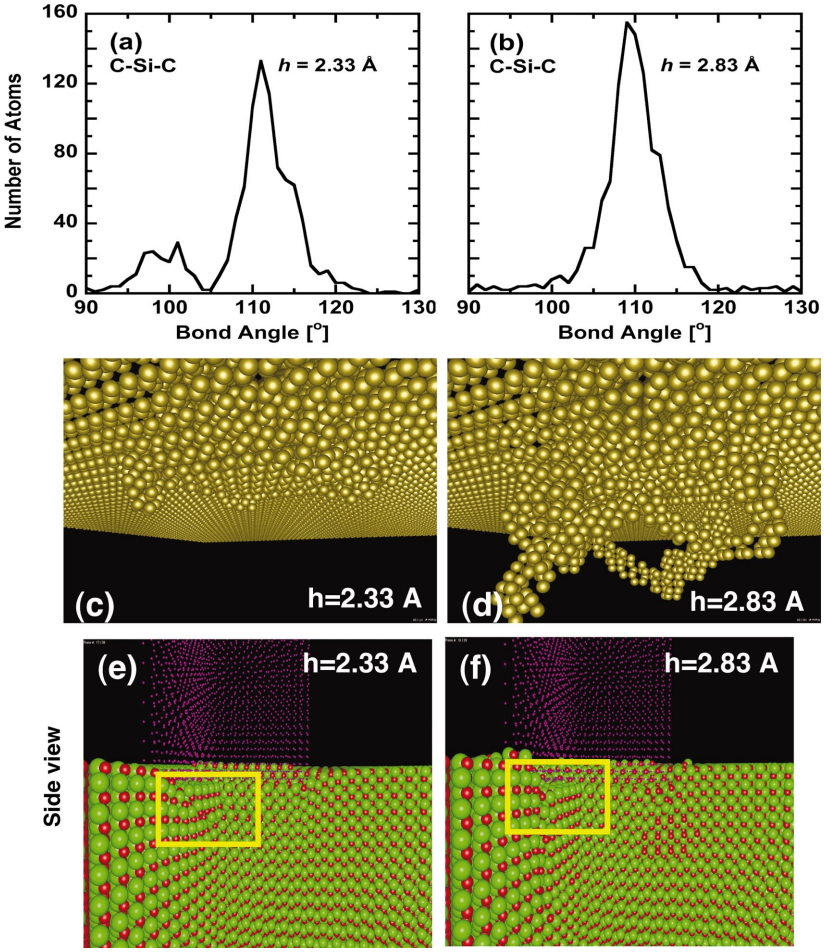

FIG. 4. (Color) Structural changes during load relaxation at $h=2.83$ Å: (a,b) Bond angle distribution of substrate atoms 12–17 Å below the initial surface at indenter depths $h=2.33$ Å and $h=2.83$ Å. (c,d) Atoms with non-three fold rings at $h=2.33$ Å and $h=2.83$ Å. (e,f) 3/4 cut showing atomic species under the indenter at $h=2.33$ Å and $h=2.83$ Å. Green spheres represent atoms of Si; red ones, C; and magenta dots represent the indenter atoms. Bending and slip of atomic layers are visible in the region enclosed by the yellow rectangles.

C. Characterization of structural correlations

The structure of the deformed material is analyzed in terms of the shortest-path ring distribution. A ring is defined here as the shortest closed path of alternating Si—C atomic bonds. A bond is assumed to exist between two atoms whose separation is $\leqslant 2.1$ Å. In our studies, we search for rings up to size 8. In a perfect zinc-blende crystal, each atom has 12 unique threefold rings (three atoms of Si alternately connected with three atoms of C), whereas the surface atoms have five threefold rings each. Structure deformations are reflected in occurrence of non-threefold rings. The amorphous phase for example was found to have two-, three-, four-, and fivefold rings.[43] In our studies we analyze the relation between the sudden drops of the load in the *P-h* response and the occurrence of non-threefold rings.

Structural defects are analyzed further by calculating bond angle distributions in two regions under the indenter: (i) from the initial surface of the crystal down to 12 Å below it; (ii) 12–17 Å below the surface. In order to describe the $c \rightarrow a$ transition, we examine the Si—C—Si and C—Si—C bond angle distributions. Both of these angles are peaked at $\sim 109°$ in the perfect zinc-blende structure and are significantly broadened in an amorphous phase. Additionally, the amorphous SiC exhibits a small peak at 85° in C—Si—C bond angle distribution, which is because of the presence of twofold rings (edge-sharing tetrahedra).[43]

III. RESULTS AND DISCUSSION

A. Load-displacement curve

Figure 2(a) shows the load-displacement curve of 3C—SiC computed in our indentation simulation. The curve exhibits a series of sudden drops of the load that occur at depths spaced equally by ~3 Å (i.e., at $h=2.83$ Å, 5.83 Å, 8.83 Å, and 11.33 Å). As it will be shown later, these load drops are related to breaking of subsequent atomic layers of the substrate, whose separation in the indentation (z) direction equals 3.08 Å. The indentation pressure is calculated as the load P divided by the indenter's cross-sectional area. For the cuboidal indenter P is proportional to the indentation pressure and for this reason the maximum load ($P_{\max} \approx 0.7$ μN) reached at the curve peaks does not increase with h [see Fig. 2(a)]. This is different from the case of a diamond-shaped indenter,[28] for which $P_{\max}$ is an increasing function of h due to the increased projected area. Another notable feature of the *P-h* curve is a shoulder observed at $h=0.83$ Å.

To understand the nature of this shoulder as well as of the first peak in the *P-h* response, we perform two unloading simulations: from (i) $h=1.83$ Å and (ii) $h=2.33$ Å. During unloading we pull out the indenter in the increments of 0.5 Å over $500\Delta t$; each of the increments is followed by a holding phase of $6000\Delta t$. The resulting curves are shown in Fig. 2(b). It is evident that the first unloading curve (squares) retraces

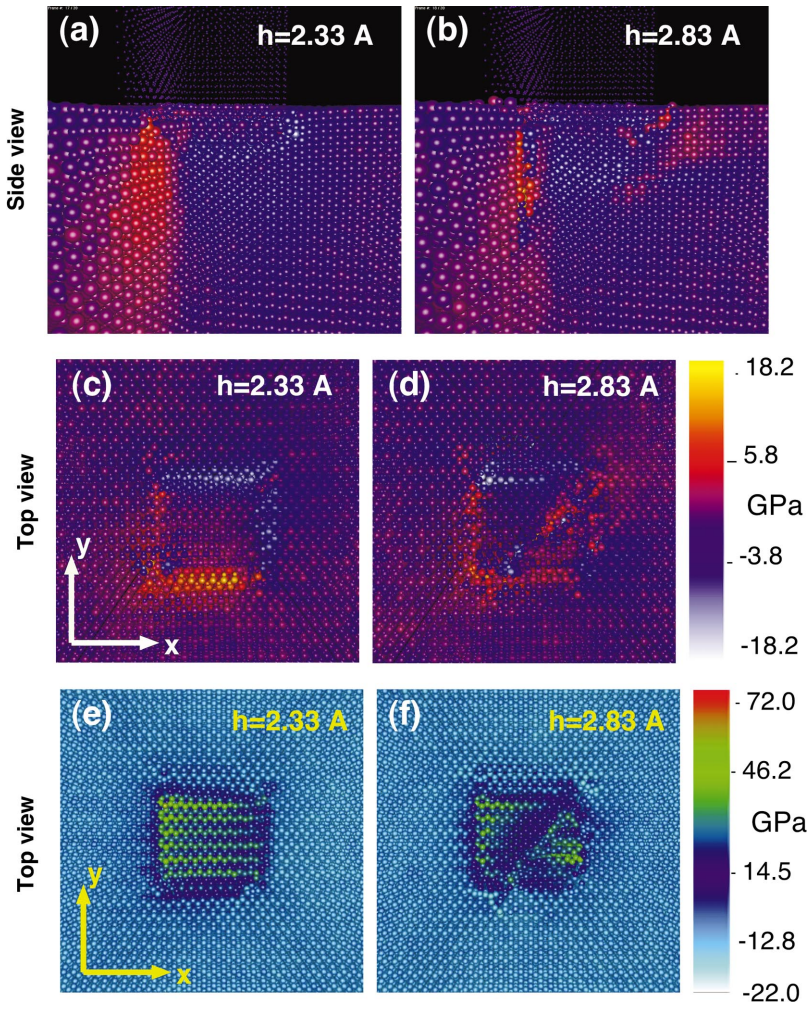

FIG. 5. (Color) Changes of shear stress and pressure (defined as in Sec. III B) during load relaxation at $h=2.83$ Å: (a,b) 3/4 cut of shear stress under the indenter at $h=2.33$ Å and $h=2.83$ Å. (c,d) Top view of shear stress at $h=2.33$ Å and $h=2.83$ Å. (e,f) Top view of the pressure at $h=2.33$ Å and $h=2.83$ Å. Small spheres represent atoms of Si; large ones, atoms of C; and blue dots in (a) and (b) correspond to indenter atoms.

exactly the loading curve (solid diamonds), and therefore the shoulder at $h=0.83$ Å is reversible. More evidence for the elastic nature of this deformation will be given in Sec. III B. The second unloading curve (circles) does not retrace the loading curve, indicating the onset of plastic deformation at $h=2.33$ Å. The corresponding load equals ~ 0.7 μN, and the yield strength of the crystal is estimated by dividing the load by the indentation area as ~ 77 GPa. It is the cuboidal shape of our indenter, which is responsible for yielding at relatively low indentation depth compared to higher displacements reached in experiments with a diamond-shaped indenter.

The shoulder and subsequent peaks in the *P*-*h* curve are analyzed in the following sections in terms of bond angle and ring distributions, atomic positions, local pressure, and direction-averaged shear stress.

B. Load relaxation at $h=0.83$ Å

The pop-in behavior of the *P*-*h* curve at $h=0.83$ Å is fully reversible, which is clear from the unloading characteristic shown in Fig. 2(b). This elastic recovery is confirmed by ring-distribution analysis. At $h=0.83$ Å we found atoms with non-threefold rings, which occur in the underlying SiC below the corners of the indenter. These rings indicate crystal deformation, and, remarkably, they disappear when the indenter is withdrawn to the depth of $h=0.33$ Å. Moreover, complete unloading of the indenter leaves no impression in the substrate.

More insight into the structural deformations is given by the bond angle distribution. When the indenter is far from the surface ($h=-5.67$ Å) there is single sharp peak at 109°, which is characteristic of a perfect tetrahedral unit in the zinc-blende crystal [see Fig. 3(a)]. Bringing the indenter closer to the surface ($h=-0.67$ Å) distorts the tetrahedral atomic arrangements centered at C or Si, thereby splitting the peak in bond angle distribution [see Fig. 3(a)]. Increasing the indentation depth ($h=0.33$ Å) results in a larger separation between the two peaks [see Fig. 3(b)]. When the depth reaches 0.83 Å, corresponding to the shoulder in the *P*-*h* curve in Fig. 2, the single-peak structure is recovered [Fig. 3(b)], which suggests the restoration of perfect tetrahedral and at least partial relaxation of indentation pressure.

Figures 3(c) and 3(d) show how this transition is reflected in the local shear stress. Atomic shear stress and pressure are calculated as $(\sigma_{xy}+\sigma_{yz}+\sigma_{zx})/3$ and $(\sigma_{xx}+\sigma_{yy}+\sigma_{zz})/3$, respectively, where $\sigma_{\alpha\beta}$ is the $\alpha\beta$ component of the stress tensor. A more quantitative description would include either the maximum shear stress on a slip plane or a direction-invariant octahedral shear stress; nevertheless, the definition of stress presented here gives a good qualitative measure of the ma-

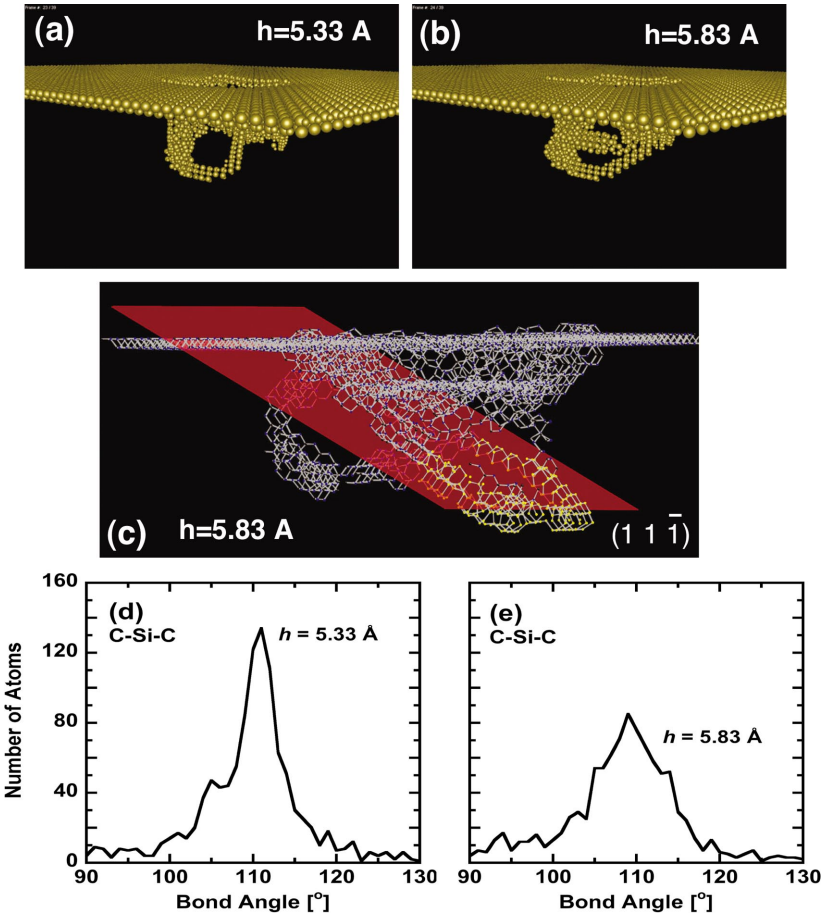

FIG. 6. (Color) Load relaxation at $h=5.83$ Å: (a,b) Atoms with non-three fold rings at $h=5.33$ Å and $h=5.83$ Å. (c) Plane $(11\bar{1})$ containing a dislocation loop shown in the ring distribution picture. (d,e) Bond angle distribution of substrate atoms 12–17 Å below the initial surface at indenter depths $h=5.33$ Å and $h=5.83$ Å.

terials response to indentation. By definition, the absolute value of shear stress is symmetric with respect to x and y axes. In Fig. 3 the light blue and orange colors correspond to the same absolute values and opposite signs, and one can see that the shear stress is nearly symmetric. The slight asymmetry is due to the particular alignment of the indenter over the substrate crystalline lattice at the atomic scale. The nonsymmetric alignment is also responsible for the difference of shear stress along x and y edges of the indenter and for the shoulder in the elastic part of the P-h response. At depths smaller than $h=0.83$ Å, atoms are pushed down and/or outward symmetrically in the $\pm x$ and $\pm y$ directions. Here atoms are pushed out from under the indenter along the x axis, and the displacements are larger in the negative x direction than in the positive one. This can be deduced from the way the local pressure is redistributed during the transition [see Figs. 3(e) and 3(f)]. Local pressure in Fig. 3(e) shows an additional feature, i.e., parallel lines of higher pressure formed along the x axis at $h=0.33$ Å. This results from the anisotropy of elastic properties in the xy plane because of different atomic layer spacing 3.08 Å and 4.36 Å in the x and y directions, respectively. Under the influence of the indentation pressure, it is easier to stretch the bonds in the y direction; hence, the ratio of atomic spacings in y and x directions is increased and the surface resembles a set of parallel lines.

C. Load relaxation at $h=2.83$ Å

Inserting the indenter beyond $h=0.83$ Å causes a distortion of tetrahedral units, which is reflected in the reappearance of two major peaks formed in bond angle distribution. At $h=2.33$Å they occur at approximately 100° and 111° [see Fig. 4(a)]. The first load relaxation in the P-h response takes place at $h=2.83$ Å at the indentation pressure almost equal to the yield strength, i.e., 77 GPa. As expected, the single peak around 109° in the bond angle distribution is recovered in the relaxed system [Fig. 4(b)].

As discussed earlier, non-three fold rings, which appear before the indenter reaches the depth of $h=2.33$ Å, disappear during unloading. The onset of plastic deformation at $h=2.33$ Å is accompanied by creation of additional non-three fold rings on atoms near the corners of the indenter [Fig. 4(c)]. Some of these rings persist even when the indenter is completely removed from the sample, suggesting that there is a correlation between ring distribution and structural deformations. Therefore, it is not surprising that the ring distribution after the load relaxation at $h=2.83$ Å [Fig. 4(d)] shows an outburst of dislocations and dislocation loops.

The side views of the atomic species under the indenter in Figs. 4(e) and 4(f) reveal that the observed load relaxation is caused by the bending of atomic layers under the indenter and their eventual slip and change of connectivity at the critical load (see the region enclosed by the yellow rectangle in the figures). During the layers bending, the shear stress is accumulated in the region of interest, as it is shown in Figs. 5(a) and 5(c). After the slip, there is a considerable release of the shear stress [Figs. 5(b) and 5(d)], which is correlated with the restoration of a single peak in the bond angle distribution

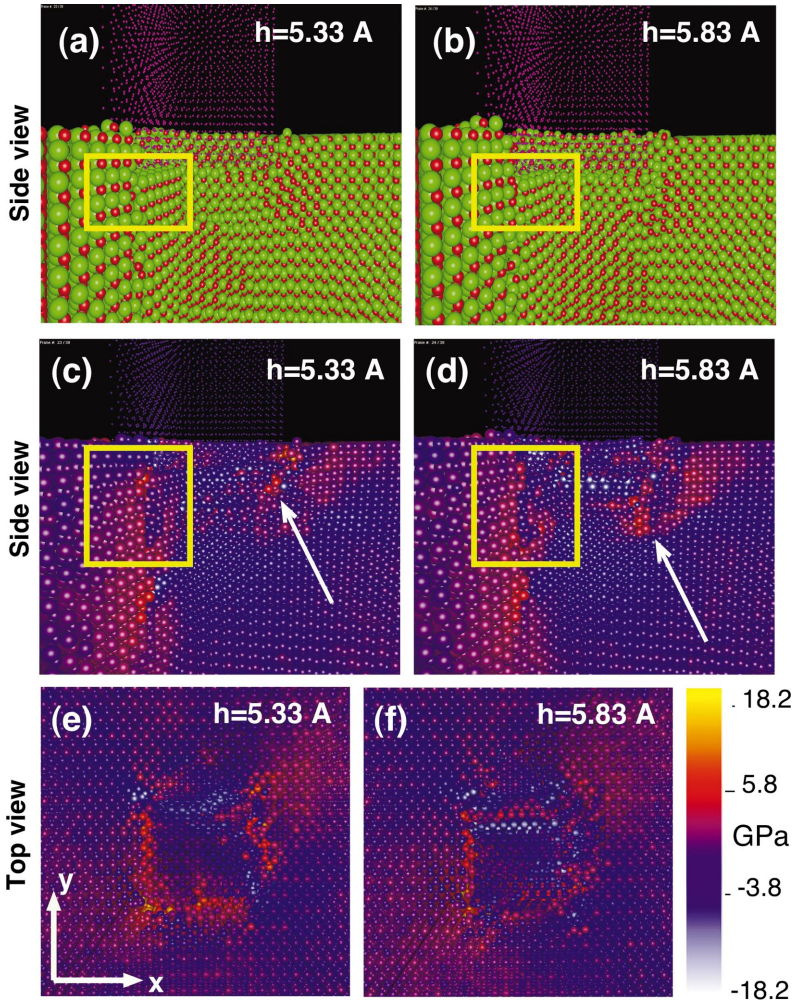

FIG. 7. (Color) Structural changes at $h=5.83$ Å: (a,b) 3/4 cut view showing atomic species at $h=5.33$ Å and $h=5.83$ Å. (c,d) 3/4 cut view showing local shear stress under the indenter at $h=5.33$ Å and $h=5.83$ Å. (e,f) Top view of shear stress at $h=5.33$ Å and $h=5.83$ Å. Small spheres correspond to atoms of Si, large ones to atoms of C, and dots in (a–d) represent atoms of the indenter. The slip of atomic layers occurs in the region marked by yellow rectangles. White arrows point to a dislocation propagating in the substrate and characterized by higher shear stress.

discussed earlier. Figures 5(e) and 5(f) show the local pressure "before" and "after" the slip. Similarly to Figs. 3(e) and 3(f) at $h=0.33$ Å, the asymmetric stretching of bonds before the slip produces lines of higher pressure (green color in the figure) along the x direction. In the surface views of shear stress [Fig. 5(d)] and the pressure [Fig. 5(f)], the dislocation emitted after the slip is manifested as a diagonal line. There is also a pile-up material that occurs on the surface along the edges of the indenter, which are the regions of high compressive pressure.[21]

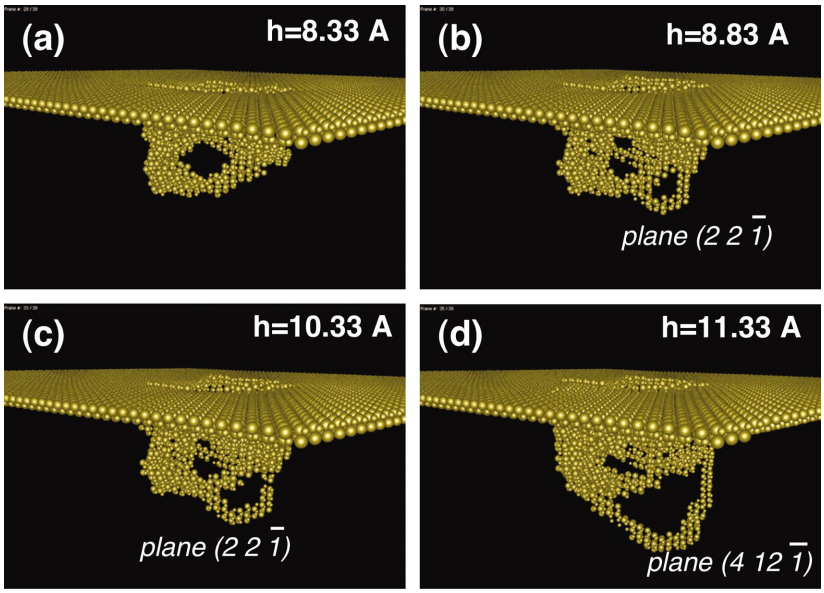

FIG. 8. (Color) Atoms with non-threefold rings at indenter depths $h=$: (a) 8.33 Å, (b) 8.83 Å, (c) 10.33 Å, and (d) 11.33 Å.

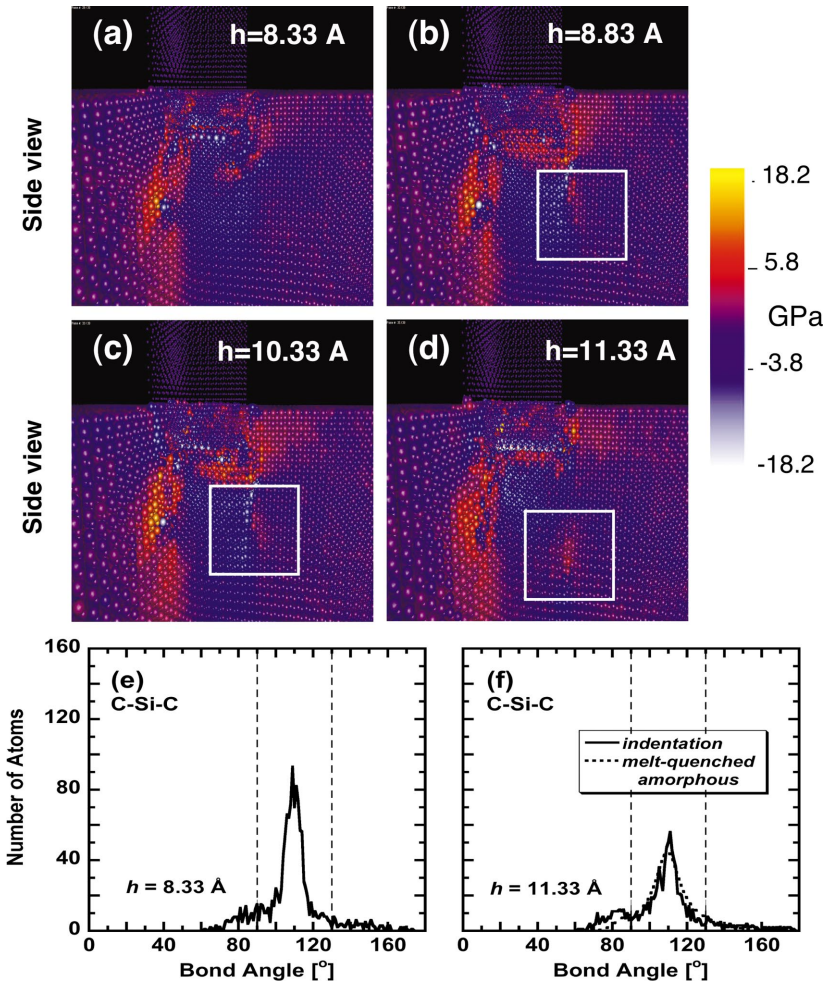

FIG. 9. (Color) 3/4 cut view of shear stress at h= (a) 8.33 Å, (b) 8.83 Å, (c) 10.33 Å, and (d) 11.33 Å. White rectangles mark regions of higher shear stress corresponding to dislocations propagating in the substrate. (e,f) Bond angle distribution of substrate atoms 12–17 Å below the initial surface at indenter depths h=8.33 Å and h=11.33 Å. The scale of the bond angle axis is different than in previous figures, where bond angle was plotted between 90° and 130°. Here we marked that region with dashed lines.

D. Load relaxation at h=5.83 Å

After the first slip of atomic layers at h=2.83 Å, the dislocations and dislocation loops emitted from the corners of the indenter slowly grow on the {111} planes, which are the glide planes of a zinc-blende crystal.[55] For instance, at h=5.33 Å, we have identified two distinct planes containing dislocation loops, i.e., (111) and $(11\bar{1})$. At h=5.83 Å another slip of the atomic layers occurs, which is accompanied by a sudden outburst of dislocations, as shown in the ring distribution in Figs. 6(a) and 6(b). In contrast to the nonoverlapping dislocation regions emanating from the corners of the indenter at h=2.83 Å, the dislocation loops here begin to merge, leaving one large loop on the $(11\bar{1})$ plane after the load relaxation [see Fig. 6(c)]. The overlapping dislocation loops generate a considerable strain under the indenter, gradually leading to amorphization. The situation is analogous to the case of irradiation-induced amorphization,[56] where low-mobility dislocation clusters coalesce, inducing a creation of amorphous domains in the crystal.

The overlapping of dislocations increases the disorder, which is reflected in the broadening of bond angle distribution in Figs. 6(d) and 6(e). Before the load relaxation [Fig. 6(d)] the main peak of the distribution is shifted to approximately 112°, and there is a smaller peak at 105°, indicating a distortion of tetrahedral atomic arrangements. After the system relaxes through slipping of atomic layers, the bond angle again is peaked around 109°, however, the distribution is significantly broadened [see Fig. 6(e)].

Figures 7(a) and 7(b) show the atomic layers before and after the slip, respectively. The corresponding side [Figs. 7(c) and 7(d)] and surface [Figs. 7(e) and 7(f)] views show the accumulation of shear stress under the indenter before the slip and its release afterwards. The stress release here is not as pronounced as at h=2.83 Å. The weaker stress relaxation is also manifested in the P-h response (Fig. 2) as a smaller drop of the load as compared to h=2.83 Å. This may be related to the presence of the back stress because of dislocations nucleated earlier, which acts as resistance to dislocation motion.[29] This back stress also prohibits a full recovery of the perfect tetrahedral structure, resulting in a broader bond angle distribution [Fig. 6(e)]. In the side view of shear stress [Figs. 7(c) and 7(d)] the dynamics of dislocations and dislocation loops is also reflected in the downward motion of the regions of high local stress (indicated by a white arrow).

E. Load relaxation at h=8.83 Å and h=11.33 Å and amorphization

The load-displacement curve between h=5.83 Å and h=8.33 Å is accompanied by gradual growth of dislocation loops on the glide planes, such as that shown in Fig. 6(c). In

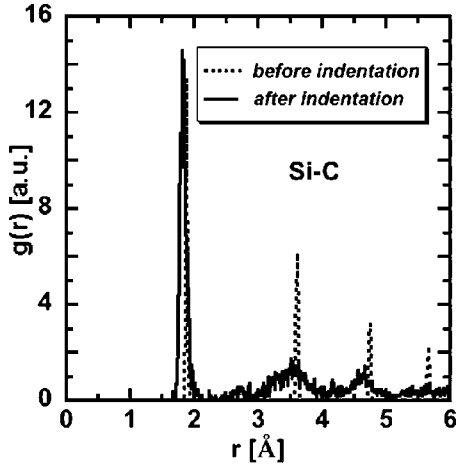

FIG. 10. Radial distribution function $g_{\alpha\beta}(r)$ before (dotted line) and after (solid line) indentation in the substrate 12–17 Å below the initial surface.

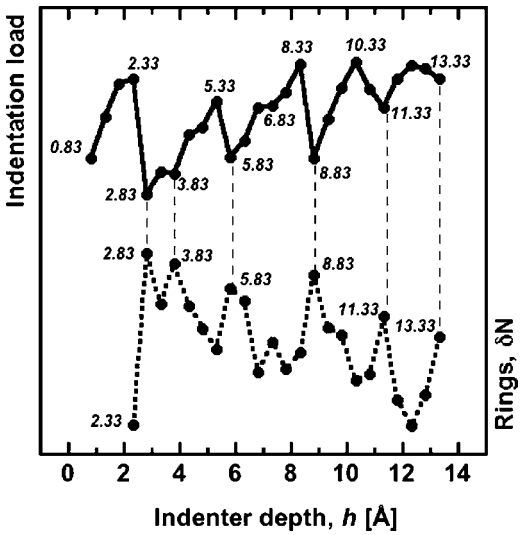

FIG. 11. Load-displacement curve $P(h)$ (solid line) and number $\delta N(h)$ of atoms with non-threefold rings (dotted line).

this range of h, there was no significant recovery of a single peak in bond angle distribution. The next considerable load relaxation takes place at $h=8.33$ Å, where the indentation pressure reaches its critical value (Fig. 2), leading to a slip of atomic layers similar to those found at smaller depths.

At the indentation depths between $h=8.33$ Å and 11.33 Å, we observe remarkable dislocation activities in the solid (see Fig. 8). At $h=8.83$ Å a dislocation line appears along the $[\bar{1}1\bar{1}]$ direction on the surface, originating at one corner of the indenter. Simultaneously, there is a loop formed on the $(22\bar{1})$ plane as shown in Figs. 8(a) and 8(b). Further increase in the indentation depth invokes the motion of dislocation loops on the $(22\bar{1})$ plane [Fig. 8(c)] until h reaches 10.33 Å. At this point the indentation pressure reaches its critical value again (Fig. 2), and more dislocations are suddenly emitted from under the indenter. As shown in Fig. 8(d), these newly created dislocations are absorbed by an existing loop to form a new one on the $(4121\bar{)}$ plane. At the same time a second dislocation line in the $[\bar{1}\bar{1}\bar{1}]$ direction is created at another corner of the indenter and propagates on the surface of the substrate.

In Figs. 9(a)–9(d) we present changes of shear stress between $h=8.33$ Å and 11.33 Å. White rectangles mark the region with increased dislocation activity, where the dislocation loops are present in Fig. 8. One can clearly see that the motion of the loops corresponds to a high-stress region moving downward.

Figures 9(e) and 9(f) show bond angle distributions at $h=8.33$ Å and 11.33 Å, respectively. Hardly any change is observed in the distribution while the indenter's position is lowered down to $h=11.33$ Å [Fig. 9(f)]. For comparison we also plotted the bond angle distribution for a melt-quenched bulk amorphous (a-SiC) system in Fig. 9(f). The a-SiC consisting of 5324 Si and 5324 C atoms (10 648 particles) was simulated with MD method. PBC were applied in all directions, and the equations of motion were integrated using the velocity-Verlet algorithm with a time step equal to 1.5 fs. Starting at the crystalline zinc-blende structure (with a density $\rho=3.2175$ g/cm^3), the system was gradually heated until the diffusion of each species was observed. At this temperature we expanded the volume by 10% ($\rho=2.896$ g/cm^3), and the system was allowed to thermalize for 50 000 time steps. The temperature of this well-thermalized liquid was lowered by successive cooling and thermalization schedules, until an amorphous phase at 300 K was obtained. The two curves for a-SiC and the material under the indenter in Fig. 9(f) are very similar, which suggests that the area under the indenter has become amorphous. For both systems the bond angle is widely distributed in the range from 70° to 160°, which is associated with various configurations and bonds formed in amorphous SiC.

In order to show the transformation from crystalline to amorphous structure, in Fig. 10 we plot the radial distribution function $g_{\mathrm{SiC}}(r)$ in the region 12–17 Å below the initial surface. The dotted curve corresponds to zinc-blende crystal before indentation. The solid curve shows $g_{\mathrm{Si—C}}(r)$ after indentation (at $h=11.33$ Å), which resembles the radial distribution function of a bulk amorphous.[43]

F. Rings versus load-displacement response

We showed earlier that every time the load dropped in the P-h curve, there was an outburst of new dislocations emitted in the system (see Figs. 4, 6, and 8). The ring distribution provides a clear picture of dislocation loops, allowing one to identify their glide planes as well as to distinguish between elastic and plastic deformation (during unloading). To quantify the correlation between the ring distribution and the P-h curve, we calculate the number $N(h)$ of atoms with non-threefold rings as a function of indentation depth. The calculated number is an increasing function of h with superimposed detailed structure. The linear increase of the curve is due to atoms surrounding the indenter, whose area of contact with the substrate is proportional to h. To study the correlation between the subsurface deformations and the ring distribution, we subtracted from $N(h)$ a linear term Ah and plotted

the resulting curve, $\delta N(h) = N(h) - Ah$, together with the load-displacement function (see Fig. 11). Here the parameter A is determined to best fit the linear part of $N(h)$. In the figure the critical depths are marked with vertical lines to show the high correlation between the two curves. Evidently, load drops are accompanied by an increase in the number of atoms with non-threefold rings, and this correlation makes ring analysis a powerful tool to study nanoindentation deformations.

IV. SUMMARY

We have performed MD simulations on a parallel computer to study the atomistic mechanisms controlling the indentation-induced crystalline-to-amorphous transition in 3C-SiC. The calculated load-displacement response shows a shoulder, which is fully reversible upon unloading. We have shown evidence that the defect-stimulated growth and dynamics of dislocation loops is responsible for the crystalline-to-amorphous transition. We have also shown how the load drops observed in the load-displacement response are related to crystalline structure and to dislocation activities under the surface. We have described the evolution of indentation damage and defect accumulation in terms of bond angles, local pressure, local shear stress, and spatial rearrangements of atoms. Finally, we have employed shortest-path ring analysis to characterize nanoindentation induced structure transformations.

ACKNOWLEDGMENTS

This work was supported by AFOSR: DURINT USC-Berkeley-Princeton, AFRL, ARL, ARO:MURI, DARPA: PROM, DOE, and NSF. Simulations were performed at the Collaboratory for Advanced Computing and Simulations and HPC at the University of Southern California, and at DoD's Major Shared Resource Centers under DoD Challenge and CHSSI projects. The authors wish to thank P. Branicio for providing the program to analyze ring structure of amorphous materials and A. Sharma for providing visualization tools.

[1] W. C. Trew, J.-B. Yan, and P. M. Mock, Proc. IEEE **79**, 598 (1991).
[2] K. Yamada and M. Mohri, in *Silicon Carbide Ceramics—1*, edited by S. Somiya and Y. Inomata (Elsevier, London, 1991).
[3] N. G. Hingorani and K. E. Stahlkopf, Sci. Am. **269**, 78 (1993).
[4] M. Bhatnagar and B. J. Baliga, IEEE Trans. Electron Devices **40**, 645 (1993).
[5] J. Baliga, Proc. IEEE **82**, 1112 (1994).
[6] W. C. Nieberding and J. A. Powell, IEEE Trans. Ind. Electron. **29**, 103 (1982).
[7] S. J. Przybylko, American Institute of Aeronautics and Astronautics, Washington, DC, Report, June, 1993.
[8] G. L. Harris, EMIS Datareviews Series (Inspec, London) 13 (1995).
[9] R. C. Marshall, J. F. Jr., and C. E. Ryan, Silicon Carbide, edited by R. C. Marshall and J. Faust, Jr., (University of Southern Carolina Press, Columbia, SC, 1974), p. 671.
[10] J. Knap and M. Ortiz, Phys. Rev. Lett. **90**, 226102 (2003).
[11] G. S. Smith, E. B. Tadmor, and E. Kaxiras, Phys. Rev. Lett. **84**, 1260 (2000).
[12] G. M. Pharr, W. C. Oliver, and D. S. Harding, J. Mater. Res. **6**, 1129 (1991).
[13] D. R. Clarke, M. C. Kroll, P. D. Kirchner, and R. F. Coof, Phys. Rev. Lett. **60**, 2156 (1988).
[14] M. F. Doerner and W. D. Nix, J. Mater. Res. **1**, 601 (1986).
[15] W. C. Oliver and G. M. Pharr, J. Mater. Res. **7**, 1564 (1992).
[16] H. M. Pollock, *Handbook of Micro/Nano Tribology*, edited by B. Bhushan (CRC Press, New York, 321, 1995).
[17] G. M. Pharr, W. C. Oliver, and D. R. Clarke, Scr. Metall. **23**, 1949 (1989).
[18] M. Tachi, Suprijadi, S. Arai, and H. Saka, Philos. Mag. Lett. **82**, 133 (2002).
[19] Z. C. Li, L. Liu, X. Wu, L. L. He, and Y. B. Xu, Mater. Sci. Eng., A **337**, 21 (2002).
[20] J. S. Kallman, W. G. Hoover, C. G. Hoover, A. J. D. Groot, S. M. Lee, and F. Wooten, Phys. Rev. B **47**, 7705 (1993).
[21] P. Walsh, R. K. Kalia, A. Nakano, and P. Vashishta, Appl. Phys. Lett. **77**, 4332 (2000).
[22] T. F. Page, W. C. Oliver, and C. J. McHargue, J. Mater. Res. **7**, 450 (1992).
[23] A. Gouldstone, H. J. Koh, K. Y. Zeng, A. E. Giannakopoulos, and S. Suresh, Acta Mater. **48**, 2277 (2000).
[24] J. B. Pethica and W. C. Oliver, *Proceedings of Materials Research Society: Thin Films: Stresses and Mechanical Properties* 130, 13 (1989).
[25] P. Tangyunyong, R. C. Thomas, T. A. M. J. E. Huston, R. M. Crooks, and A. J. Howard, Phys. Rev. Lett. **71**, 3319 (1993).
[26] W. W. Gerberich, J. C. Nelson, E. T. Lilleodden, P. Anderson, and J. T. Wyrobek, Acta Mater. **44**, 3585 (1996).
[27] C. L. Kelchner, S. J. Plimpton, and J. C. Hamilton, Phys. Rev. B **58**, 11085 (1998).
[28] K. J. V. Vliet, J. Li, T. Zhu, S. Yip, and S. Suresh, Phys. Rev. B **67**, 104105 (2003).
[29] J. Li, K. J. V. Vliet, T. Zhu, S. Yip, and S. Suresh, Nature (London) **418**, 307 (2002).
[30] A. Gouldstone, K. J. V. Vliet, and S. Suresh, Nature (London) **411**, 656 (2001).
[31] J. A. Zimmerman, C. L. Kelchner, P. A. Klein, J. C. Hamilton, and S. M. Foiles, Phys. Rev. Lett. **87**, 165507 (2001).
[32] M. J. Buehler, F. F. Abraham, and H. J. Gao, Nature (London) **426**, 141 (2003).
[33] E. T. Lilleodden, J. A. Zimmerman, S. M. Foiles, and W. D. Nix, J. Mech. Phys. Solids **51**, 901 (2003).
[34] U. Landman, W. D. Luedtke, N. A. Burnham, and R. J. Colton, Science **248**, 454 (1990).
[35] J. Belak, D. B. Boercker, and I. F. Stowers, Mater. Res. Bull. **18**, 55 (1993).
[36] K. Komvopoulos and W. Yan, J. Appl. Phys. **82**, 4823 (1997).

[37] R. Smith, D. Christopher, and S. D. Kenny, Phys. Rev. B **67**, 245405 (2003).
[38] I. Szlufarska, R. K. Kalia, A. Nakano, and P. Vashishta, Appl. Phys. Lett. **85**, 378 (2004).
[39] V. B. Shenoy, R. Phillips, and E. B. Tadmor, J. Mech. Phys. Solids **48**, 649 (2000).
[40] E. B. Tadmor, R. Miller, and R. Phillips, J. Mater. Res. **14**, 2233 (1999).
[41] A. C. Wright and J. A. E. Desa, Phys. Chem. Glasses **19**, 140 (1978).
[42] J. P. Rino, I. Ebbsjo, R. K. Kalia, A. Nakano, and P. Vashishta, Phys. Rev. B **47**, 3053 (1993).
[43] J. P. Rino, I. Ebbsjo, P. Branicio, R. K. Kalia, A. Nakano, and P. Vashishta, Phys. Rev. B **70**, 045207 (2004).
[44] G. J. Martyna, M. E. Tuckerman, D. J. Tobias, and M. L. Klein, Mol. Phys. **87**, 1117 (1996).
[45] M. Parrinello and A. Rahman, Phys. Rev. Lett. **45**, 1196 (1980).
[46] J. R. Ray and A. Rahman, J. Chem. Phys. **82**, 4243 (1985).
[47] M. Tuckerman, B. J. Berne, and G. J. Martyna, J. Chem. Phys. **97**, 1990 (1992).
[48] P. Vashishta, R. K. Kalia, W. Li, J. Ebbsjo, *Amorphous Insulators and Semiconductors*, edited by M. F. Thorpe and M. I. Mitkova, NATO ASI, Ser. 3, Vol. 23 (Kluwer, Boston, 1996).
[49] F. H. Stillinger and T. A. Weber, Phys. Rev. B **31**, 5262 (1985).
[50] F. Shimojo, I. Ebbsjo, R. K. Kalia, A. Nakano, J. P. Rino, and P. Vashishta, Phys. Rev. Lett. **84**, 3338 (2000).
[51] A. Chatterjee, R. K. Kalia, A. Nakano, A. Omeltchenko, and K. Tsuruta, Appl. Phys. Lett. **77**, 1132 (2000).
[52] A. Taylor and R. M. Jones, in Silicon Carbide, A High Temperature Semiconductor, edited by J. R. O'Connor and J. Smliltens (Pergamon, New York, 1960), p. 147.
[53] W. R. Lambrecht, B. Segall, M. Methfessel, and M. v. Schilfgaarde, Phys. Rev. B **44**, 3685 (1991).
[54] M. Catti, Phys. Rev. Lett. **87**, 035504 (2001).
[55] J. P. Hirth, *Theory of Dislocations*, (Krieger, Melbourne, FL, 1992).
[56] F. Gao and W. J. Weber, Phys. Rev. B **66**, 024106 (2002).